

# Flexible PT-Symmetric Optical Metasurfaces

**Nye, N. S.; Halawany, A. E.; Markos, Christos; Khajavikhan, M.; Christodoulides, D. N.**

*Published in:*
Physical Review Applied

*Link to article, DOI:*
10.1103/PhysRevApplied.13.064005

*Publication date:*
2020

*Document Version*
Publisher's PDF, also known as Version of record

# Flexible $\mathcal{PT}$-Symmetric Optical Metasurfaces

N. S. Nye,[1,*] A. E. Halawany,[1] C. Markos,[2] M. Khajavikhan,[1] and D. N. Christodoulides[1]

[1] *College of Optics & Photonics—CREOL, University of Central Florida, Orlando, Florida 32816, USA*

[2] *DTU Fotonik, Department of Photonics Engineering, Technical University of Denmark, DK-2800 Kgs. Lyngby, Denmark*

(Received 31 May 2019; revised manuscript received 30 March 2020; accepted 15 April 2020; published 2 June 2020)

The synthesis of ultrathin photonic structures in order to effectively redirect and mold optical wave fronts into arbitrary shapes is of crucial importance in modern beam steering, imaging, and sensing technologies. To this end, planar subwavelength systems such as optical metasurfaces have been intensely investigated in recent years. Such arrangements rely on abrupt, yet controllable, phase shifts imparted on the incident beam, by means of judiciously designed anisotropic nanoantennas. Here, we propose and demonstrate an altogether different methodology in order to manipulate the flow of light, by adopting a diatomic parity-time ($\mathcal{PT}$)-symmetric Bravais-lattice topology, the unit cell of which involves only a transparent and a lossy optical component. In this respect, a honeycomblike configuration is employed, the principal symmetries of which are progressively broken through specific geometric transformations. The complex near-field coupling interactions between neighboring diffractive elements give rise to a discerning enhancement or attenuation along specific directions in the far field, over a broad range of wavelengths in the visible domain. In this work, we report the realization of an all-passive $\mathcal{PT}$-symmetric optical metasurface on a flexible polyimide substrate, capable of demonstrating selective directional scattering. Our study draws a clear connection between surface topology and radiation directivity, which can be systematically utilized toward observing unconventional transport effects in flat- and curved-space $\mathcal{PT}$ lattices.

DOI: 10.1103/PhysRevApplied.13.064005

## I. INTRODUCTION

The advent of metasurfaces has inspired intense research activity in the field of planar photonics. In such systems, a gradual phase shift can be imposed on the incident optical wave front, thus leading to a generalized version of Snell's law [1–3]. The inherent ability of metasurfaces to control the phase, polarization, and angular momentum of the incident light via surface-confined subwavelength nanofeatures has made such artificial structures of great interest for a number of applications [4–8], aimed toward scalable refractive or diffractive optical components. In recent years, parity-time synthetic photonic arrangements have also been the subject of extensive investigation [9–11]. Such $\mathcal{PT}$-symmetric concepts—originally conceived within the context of quantum field theories—provide a means of constructing alternative classes of non-Hermitian Hamiltonians, capable of exhibiting entirely real eigenvalue spectra. Given that, in optics, the complex refractive index $n(r)$ plays the role of a quantum mechanical potential $V(r)$, one may then conclude that in a photonic setting, $\mathcal{PT}$ symmetry requires that the following condition is fulfilled: $n(r) = n^*(-r)$. In other words, the real part of the refractive index must be an even function of position, while the imaginary component, denoting gain or loss, must be antisymmetric. In more general arrangements, where the problem must be treated electrodynamically [12], this same symmetry implies that the complex permittivity satisfies $\epsilon(r) = \epsilon^*(-r)$.

The nontrivial interplay between gain and loss domains in non-Hermitian platforms has led to a number of exciting possibilities that have no counterpart in Hermitian environments. These include, for example, power oscillations, scattering elimination, nonreciprocal light propagation, and exceptional-point dynamics, to name a few [13–19]. The anomalous scattering properties of such systems—resulting from an underlying spontaneous symmetry-breaking mechanism—have been considered within the context of $\mathcal{PT}$-symmetric metasurfaces. So far, the potential of these arrangements has been the subject of mostly theoretical studies and applications have been proposed for electromagnetic cloaking, subwavelength sensing, and planar focusing [20–24]. While asymmetric light transport and violation of Friedel's law have been reported in one-dimensional diffraction settings [25–28], the more complex analogs of these effects in higher-dimensional free-space optical platforms still remain experimentally elusive.

In this paper, we experimentally observe directional far-field scattering by exploiting the geometric distortion

*nnye@knights.ucf.edu

 

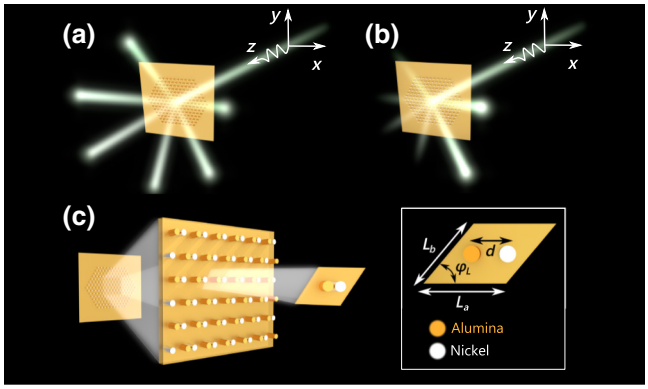


FIG. 1. A passive $\mathcal{PT}$-symmetric metasurface. (a) The symmetric far-field emission in various diffraction modes under Hermitian conditions (alumina nanopillars). (b) The lopsided diffraction and loss-induced redistribution of power in favor of desired free-space modes for the $\mathcal{PT}$-symmetric case (involving alumina and nickel nanopillars). (c) A schematic illustration of an irregular $\mathcal{PT}$-symmetric photonic honeycomb network. The inset shows the unit cell of a generalized oblique Bravais-lattice topology.

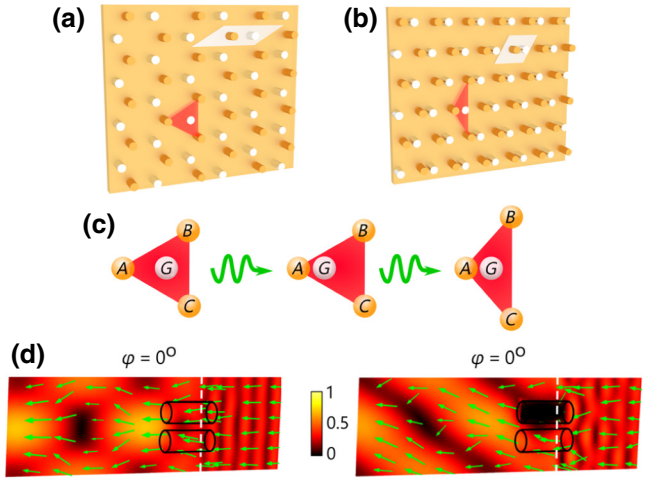


FIG. 2. The operation principle of $\mathcal{PT}$-symmetric metasurfaces. (a),(b) Standard (a) and "deformed" (b) honeycomb networks. The respective unit cells (white) and triangles (red) formed by neighboring diffractive elements are also shown. (c) Sequential geometric transformations relating the lattices in (a) and (b). Elements $A$, $B$, and $C$ indicate the position of lossless sapphire nanopillars, while $G$ denotes lossy nickel elements. (d) Near-field results for the Hermitian (left panel) and $\mathcal{PT}$-symmetric (right panel) cases. The arrows indicate the Poynting-power-density-vector flow, while the near-field distributions are depicted along the azimuthal planes $\phi = 0^\circ$.

associated with the underlying surface topology of a previously unexplored family of irregular photonic honeycomb arrangements (Fig. 1). The proposed $\mathcal{PT}$-symmetric dimer model relies on deeply subwavelength near-field interactions between a lossy diffractive element and its transparent counterpart. In this manner, we demonstrate robust control over the propagating free-space modes and a pronounced unidirectionality. As with passive non-Hermitian waveguide arrangements, where loss-induced transparency is possible [14], in the present work we report loss-induced enhancement or suppression of radiation toward specific directions of interest in the visible part of the spectrum. The "deformed" honeycomb network used in this study is depicted in Fig. 1(c). This system stems from a general class of diatomic oblique Bravais lattices [inset of Fig. 1(c)] with unit-cell dimensions $L_a$ and $L_b$, while $d$ and $\phi_L$ represent the scatterer center-to-center distance and the lattice angle, respectively. We note that this diffractive arrangement respects both local, as well as global, $\mathcal{PT}$ symmetry.

## II. PRINCIPLE OF OPERATION

Figure 2(a) depicts a regular honeycomb array of scatterers with $L_a = 3d$, $L_b = d\sqrt{3}$, and $\phi_L = 30^\circ$. Such a configuration is characterized by a perfect hexagonal tiling, which, in turn, dictates an angularly balanced and nondirectional far-field radiation pattern (see Sec. S.I in the Supplemental Material [29]). In order to attain directional scattering, certain lattice symmetries need to be progressively broken, as illustrated in Fig. 2(c). More specifically, we modify the topology of the $ABC$ triangle, formed by the neighboring nanopillars of the two-dimensional (2D) periodic structure. If the network is of the honeycomb type, $ABC$ happens to be equilateral, with its circumcenter ($G$) occupied by another diffractive element. As a first step in altering the topology of the system, we shift the central cylinder $G$ along the perpendicular bisector of $BC$. Subsequently, $ABC$ is rescaled and $A$ is relocated, such that $AB = AC \neq BC$. As a result, we obtain an irregular "deformed" honeycomb lattice [Fig. 2(b)], for which $L_a = L_b = L$ and $\phi_L = 60^\circ$. In this case, the amount of lattice deformation in the final arrangement is determined by both displacements $\Delta G$ and $\Delta A$, and as such dictates the imbalance between the propagating modes. In Sec. S.I in the Supplemental Material [29], we provide an alternative view of the aforementioned geometric transformations, by starting from a generalized diatomic oblique Bravais unit cell. In doing so, it is shown that in order to achieve radiation directionality, both of the relations $L_a = 2L_b \cos\phi_L$ and $L_b/\{2d\cos\phi_L\} \neq 1$ must be satisfied. The former equality is required for the alignment of the lossy pillars in the $y$ direction ($y$-polarized incident electric field), while the latter condition leads to the desired lattice distortion.

Without any loss of generality, the proposed configuration is designed so as to support six distinct diffraction orders at a wavelength of $\lambda_o = 530$ nm. For this configuration, the unit cell has dimensions $L_a = L_b = 690$ nm and $\phi_L = 60^\circ$. The diameter of the nanoscatterers

is $D = 160$ nm, while their center-to-center distance is $d = 210$ nm. Due to the deeply subwavelength gap (approximately $\lambda_o/10$) between the lossy and transparent pillars, their respective coupling strengths become enhanced, thus leading to a highly asymmetric radiation profile. In order to further increase such near-field interactions, the nanopillars (overall height $h = 370$ nm) are partially buried at a height of $h_s = 90$ nm in the polyimide substrate. In all cases, nickel [30] (Ni) is used for realizing the lossy elements, alumina (or sapphire) [31] ($Al_2O_3$) for the transparent scatterers, and high-index polyimide [32]. for the substrate. Moreover, it is assumed that the optical field is $y$-polarized at normal incidence. The propagation direction of the transmitted modes is determined by the elevation and azimuth angles $\theta_d$ and $\phi_d$, respectively, which can be analytically computed (see Appendix A).

Figure 2(d) depicts near-field simulation results along the azimuthal cross-section plane at $\phi = 0^\circ$, associated with the Hermitian and its corresponding $\mathcal{PT}$-symmetric arrangement, for a wavelength of $\lambda_o = 530$ nm. In the $\mathcal{PT}$-symmetric configuration [right panel—Fig. 2(d)], the Poynting-vector graphs clearly indicate a reorientation of the average power flow toward the lossy diffractive nanopillars, in direct contrast to the Hermitian case [left panel—Fig. 2(d)]. This lopsided emission constitutes a clear violation of Friedel's law of diffraction and is attributed to the presence of an additional transverse component in the Poynting-vector field, needed to promote energy transfer to the lossy subdomains. While analogous effects can take place for potentials with asymmetric loss distributions (see anomalous scattering in atomic and/or molecular crystals—[33]), nevertheless in the present work we aim to maximize the lopsidedness of the far-field diffraction pattern by capitalizing on the passive $\mathcal{PT}$-symmetric arrangement of the nickel nanopillar losses. For this purpose, a systematic investigation (including numerical simulations and theoretical calculations) is performed in Appendix B, which indicates that the optimum operation of the flexible metasurface (i.e., maximal asymmetry in light transport) takes place at the $\mathcal{PT}$-symmetry-breaking transition point ($\Delta\kappa/\Delta n = 1.7$) for a broad range of wavelengths. Given the material properties of nickel and alumina, the contrast ratio between the real—$\Delta n$ and imaginary—$\Delta\kappa$ parts of the refractive-index modulation becomes $\Delta\kappa/\Delta n \sim 4.3$, which guarantees operation in the broken-$\mathcal{PT}$-phase regime. The 2D field distributions along the plane $\phi = 90^\circ$ are also provided in Sec. S.I in the Supplemental Material [29]. In this case, no asymmetry is observed owing to the alignment of the lossy pillars along the $y$ axis.

## III. EXPERIMENTAL METHODS

For our study, we fabricate an irregular photonic honeycomb lattice via a double-patterning process using standard electron-beam ($e$-beam) lithography techniques. A layer of silica ($SiO_2$) with a thickness of 300 nm is deposited on a silicon wafer ($2 \times 3$ cm$^2$) via plasma-enhanced chemical-vapor deposition (PECVD). Consequently, the sample is spin coated with a polymethyl methacrylate (PMMA) 950 A6 film for an additional thickness of 600–630 nm through a gradual process (see Sec. S.III in the Supplemental Material [29]) and baked in the furnace at 180°C for 15 h. The first $e$-beam lithography step follows, with the respective $e$-beam writing parameters (dosage, size, and separation) provided in Table S1 in the Supplemental Material [29], for both the Hermitian and $\mathcal{PT}$-symmetric cases. Subsequently, alumina (passive arrangement) or nickel (non-Hermitian configuration) is deposited with a thickness of 370 nm at a rate of 1 Å/s. Lift-off with acetone is performed, while isopropanol (IPA) is used to remove any residual material. Images taken under the optical microscope are shown in Fig. S7 in the Supplemental Material [29], after drying the sample with $N_2$ gas. For the $\mathcal{PT}$-symmetric metasurface, an additional $e$-beam lithography step is required for the patterning of the $Al_2O_3$ pillars. This again involves the spin coating of a thin PMMA film, followed by $e$-beam writing at a dosage of 760 $\mu$C/cm$^2$, using a separation of 80 nm and a size of 110 nm. Alumina is then deposited with a thickness of 370 nm (at 1 Å/s). During the $Al_2O_3$ deposition process, the temperature of the chamber increases, thus causing the PMMA to be hardened. Therefore, the polymer is exposed to ultraviolet radiation for 6 min to soften it. After the lift-off process is completed, polyimide is spin coated on both the passive and $\mathcal{PT}$-symmetric arrangements [1000-rpm (revolutions per minute) speed at 100-rpm acceleration, for 60 s], in order to attain a uniform polyimide film of 10-$\mu$m thickness. Finally, dry and wet etching (buffer oxide) are both performed, in order to remove the silicon substrate and the silica sacrificial layer, respectively. The end result is a flexible Hermitian–$\mathcal{PT}$-symmetric metasurface, as shown in Figs. 3(a) and 3(b). Scanning-electron-microscope (SEM) images of this irregular hexagonal pattern formation are shown in Figs. 3(c) and 3(d).

## IV. RESULTS

In order to probe the far-field scattering behavior of these $\mathcal{PT}$-symmetric metasurfaces, we illuminate the samples with a laser beam at 530 nm, after passing through a vertical polarizer (see Sec. S.III in the Supplemental Material [29]). In the case of the broadband light source, a biconvex lens is also used, after an aperture, in order to collimate light. The experiment is performed under normal incidence, while the power of the diffracted orders is measured using a power meter. The field directivity of the fabricated samples is quantified by means of an extinction ratio, defined as the ratio between the power efficiencies of the attenuated and enhanced propagating

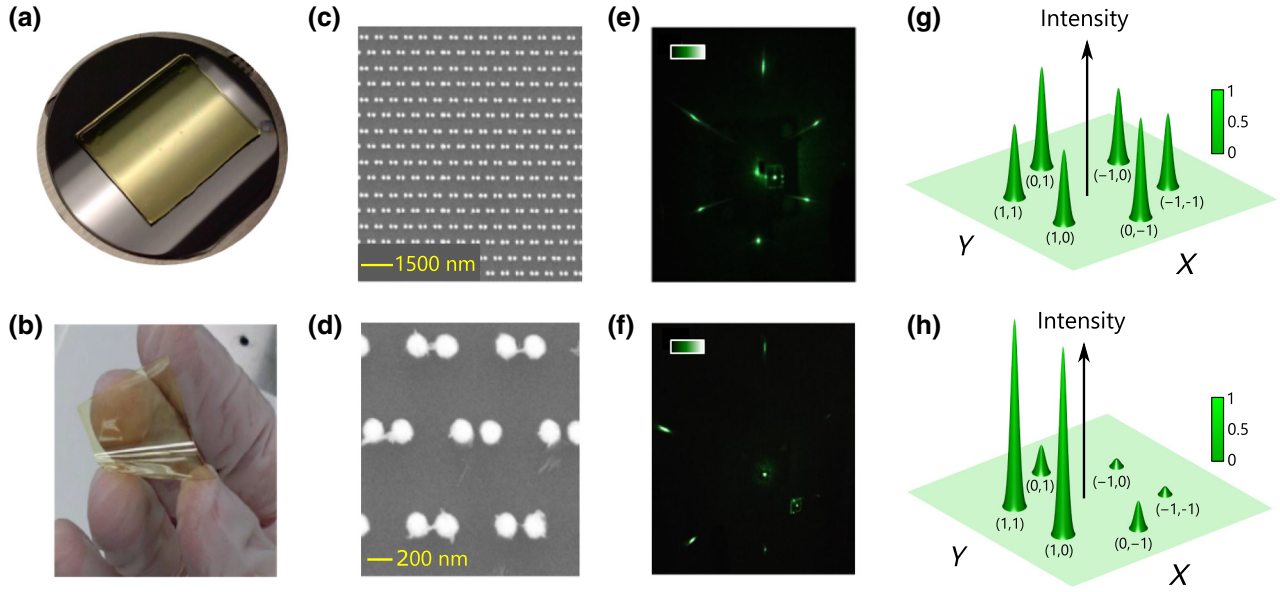


FIG. 3. The experimental results. (a),(b) A flexible $\mathcal{PT}$-symmetric metasurface on Si substrate (a) and a final sample with the Si etched away (b). (c),(d) SEM images of the irregular hexagonal pattern on the flexible substrate. (e),(f) Far-field emission under Hermitian (e) and parity-time (f) conditions. (g),(h) The experimentally measured power-diffraction efficiencies for the Hermitian (g) and $\mathcal{PT}$-symmetric (h) configurations.

modes. As previously mentioned, the structure supports six higher-order transmission modes with respective azimuth angles $\phi_d = \pm 30^\circ, \pm 90^\circ$, and $\pm 150^\circ$. In all cases, the elevation angle of propagation is $\theta_d = 62^\circ$. The obtained results [Figs. 3(e)–3(h)] demonstrate a pronounced lopsided diffraction, as predicted theoretically. The large value of the ratio $\Delta\kappa/\Delta n \sim 4.3$ guarantees operation in the broken $\mathcal{PT}$ phase, which in turn implies highly asymmetric light transport (see Appendixes B and [19]). The numerically computed (Supplemental Material, Sec. S.I [29]) and experimentally obtained far-field efficiencies [Figs. 3(g) and 3(h)] are found to be in good agreement. More specifically, mode orders $(0, 1)$, $(0, -1)$, $(-1, 0)$, and $(-1, -1)$ are reduced below 1%, while the propagating modes, $(1, 1)$ and $(1, 0)$, become significantly enhanced by a factor of $\times 2.3$, leading to an extinction ratio of $-8$ dB. Such unidirectional emission indicates a broken $\mathcal{PT}$ phase and signifies a clear violation of Friedel's law of diffraction. Moreover, the observed loss-induced enhancement of the desired modes is a unique characteristic of passive $\mathcal{PT}$-symmetric structures operating close to their exceptional point (see Ref. [14]).

Finally, in order to demonstrate that this metasurface is indeed broadband, we illuminate the sample with an incoherent white-light source with spectral response in the range 410–590 nm (see Sec. S.II in the Supplemental Material [29]). The corresponding results are shown in Fig. 4 and demonstrate a suppression of all the free-space modes, besides the desired orders $(1, 1)$ and $(1, 0)$, with a respective extinction ratio of $-6$ dB. Detailed numerical calculations of the far-field efficiencies are performed in Sec. S.II in the Supplemental Material [29] and once again indicate a close match between experiments and simulations. We should note that in all cases, the two diffraction orders propagating in the $\phi = 90^\circ$ plane, i.e.,

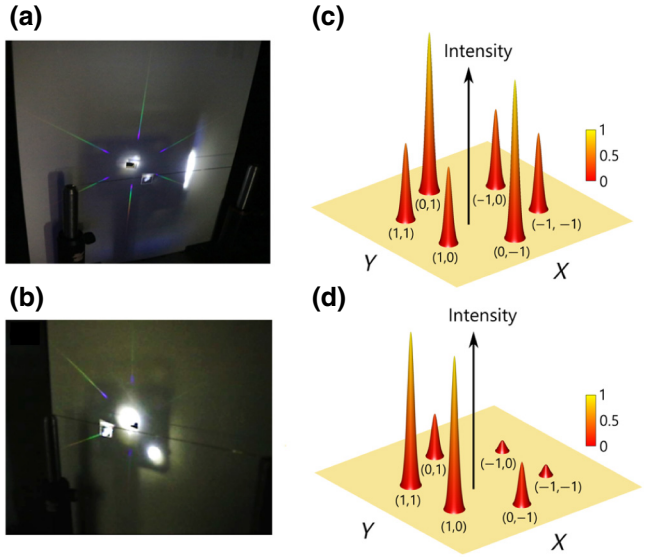


FIG. 4. The broadband scattering results. (a),(b) The far-field diffraction patterns under Hermitian (a) and $\mathcal{PT}$ conditions (b). (c),(d) The power-diffraction efficiencies, as measured experimentally, for the Hermitian (c) and $\mathcal{PT}$-symmetric (d) metasurfaces.

$(0, 1)$ and $(0, -1)$, are equally attenuated, owing to the imposed alignment of the lossy nanopillars along the $y$ direction. Once again, the flexible metasurface operates in the broken-$\mathcal{PT}$-phase regime, owing to the large value of the contrast ratio ($\Delta\kappa/\Delta n > 4$) over the wavelength range of interest, 410–590 nm (see Appendix B).

## V. CONCLUSION

In this work, we show that flexible $\mathcal{PT}$-symmetric metasurfaces can be employed to significantly enhance or suppress their respective far-field diffraction efficiencies. Passive $\mathcal{PT}$-symmetry is introduced in oblique diatomic Bravais lattices though loss elements. The presented methodology can be readily extended to other wavelength regions (e.g., terahertz and infrared) and physical settings, such as acoustics and microwaves. Moreover, our approach can open up alternative possibilities in the field of reconfigurable optics, based on materials with controllable properties via external stimuli, such as voltage, temperature, and magnetic fields. Finally, our findings could pave the way toward flexible photonic metasurfaces and inspire further investigations on alternative transport mechanisms resulting from 2D flat or curved parity-time synthetic lattice topologies.

## ACKNOWLEDGMENTS

This work was supported by the Office of Naval Research (Grant No. N00014-18-1-2347), the Army Research Office (Grant No. W911NF-17-1-0481), the U.S.–Israel Binational Science Foundation (Grant No. 2016381), Texas A&M University (Grant No. NPRP9-020-1-006), the Penn State University Materials Research Science and Engineering Center (MRSEC), Center for Nanoscale Science (Grant No. 1420620), and the Air Force Office of Scientific Research (Grant No. FA9550-14-1-0037). N.S.N. is grateful for funding from the Alexander S. Onassis Public Benefit Foundation and the Foundation for Education and European Culture. We would also like to acknowledge important infrastructure provided for this work by the Nano Research Facility (NRF) at the University of Florida (UF).

## APPENDIX A: SCATTERING ANALYSIS FOR AN OBLIQUE BRAVAIS LATTICE

The unit-cell vectors, describing an oblique Bravais-lattice topology with lattice-angle dimensions $L_\alpha \times L_b$ (see Fig. S1 in the Supplemental Material [29]), are given by $\boldsymbol{\alpha}_1 = L_\alpha \mathbf{x}$ and $\boldsymbol{\alpha}_2 = L_b\{\cos(\phi_L)\mathbf{x} + \sin(\phi_L)\mathbf{y}\}$. Following the analysis for a three-dimensional periodic arrangement, the reciprocal lattice vectors will be given by $\mathbf{G}_1 = 2\pi(\boldsymbol{\alpha}_2 \times \boldsymbol{\alpha}_3)/\{\boldsymbol{\alpha}_1 \cdot (\boldsymbol{\alpha}_2 \times \boldsymbol{\alpha}_3)\} = 2\pi\{\mathbf{x} - \cot(\phi_L)\mathbf{y}\}/L_\alpha$ and $\mathbf{G}_2 = 2\pi(\boldsymbol{\alpha}_3 \times \boldsymbol{\alpha}_1)/\{\boldsymbol{\alpha}_2 \cdot (\boldsymbol{\alpha}_3 \times \boldsymbol{\alpha}_1)\} = 2\pi \csc(\phi_L)\mathbf{y}/L_b$, where $\boldsymbol{\alpha}_3 = \mathbf{z}$. The incident wave vector can be expressed as $\mathbf{k}_i = k_o n_1\{\sin(\theta_i)\cos(\phi_i)\mathbf{x} + \sin(\theta_i)\sin(\phi_i)\mathbf{y} + \cos(\theta_i)\mathbf{z}\}$, where $k_o$ is the free-space wave number, $n_1$ represents the refractive index of the incident medium, and $\theta_i$ and $\phi_i$ denote the elevation and azimuth angles of the electromagnetic wave, respectively. The phase-matching condition dictates that $\mathbf{k}_{t,\parallel} = \mathbf{k}_{i,\parallel} + n\mathbf{G}_1 + m\mathbf{G}_2$, where $(n, m)$ indicates the propagating order, while $\mathbf{k}_{i,\parallel}$ and $\mathbf{k}_{t,\parallel}$ represent the tangential components of the incident and diffracted wave vectors, correspondingly. Consequently, we obtain

$$\mathbf{k}_{t,\parallel} = \left\{k_o n_1 \sin(\theta_i)\cos(\phi_i) + n\frac{2\pi}{L_\alpha}\right\}\mathbf{x} + \left\{k_o n_1 \sin(\theta_i) \times \sin(\phi_i) - n\frac{2\pi}{L_\alpha}\cot(\phi_L) + m\frac{2\pi}{L_b}\csc(\phi_L)\right\}\mathbf{y}. \tag{A1}$$

On the other hand, the normal component of $\mathbf{k}_t$ will be provided by $\mathbf{k}_{t,\perp} = \sqrt{(k_o n_2)^2 - \left|\mathbf{k}_{t,\parallel}\right|^2}\mathbf{z}$, where $n_2$ is the refractive index of the transmission medium and $\left|\mathbf{k}_{t,\parallel}\right|$ is the magnitude of vector $\mathbf{k}_{t,\parallel}$. In order to obtain propagating waves, $\mathbf{k}_{t,\perp}$ should be a real number. This implies that $(k_o n_2)^2 \geq \left|\mathbf{k}_{t,\parallel}\right|^2$, which leads to the inequality $\alpha_m n^2 + b_m n + c_m \leq 0$, with coefficients $\alpha_m$, $b_m$, and $c_m$ and discriminant $\Delta$, described by the following relations:

$$a_m = \left\{\frac{2\pi \csc(\phi_L)}{L_\alpha}\right\}^2, \tag{A2}$$

$$b_m = \frac{4\pi}{L_\alpha}\left\{k_o n_1 \sin(\theta_i)\cos(\phi_i) - k_o n_1 \sin(\theta_i)\sin(\phi_i)\cot(\phi_L) - m\frac{2\pi}{L_b}\cot(\phi_L)\csc(\phi_L)\right\}, \tag{A3}$$

$$c_m = -k_o^2 n_2^2 + k_o^2 n_1^2 \sin^2(\theta_i) + \left(m\frac{2\pi}{L_b}\right)^2 \csc^2(\phi_L) + m\frac{4\pi}{L_b}k_o n_1 \sin(\theta_i)\sin(\phi_i)\csc(\phi_L), \tag{A4}$$

$$\Delta = -4\csc^2(\phi_L)\left(\frac{2\pi}{L_\alpha}\right)^2\left(\frac{2\pi}{L_b}\right)^2 \left\{m - \frac{L_b}{\lambda}\{-n_1 \sin(\theta_i)\cos(\phi_L - \phi_i) + n_2\}\right\} \left\{m - \frac{L_b}{\lambda}\{-n_1 \sin(\theta_i)\cos(\phi_L - \phi_i) - n_2\}\right\}. \tag{A5}$$

Since $\alpha_m \geq 0$, it should be true that $\Delta \geq 0$, which yields the following constraints for parameters $n$ and $m$:

$$\frac{L_b}{\lambda}\{-n_1 \sin(\theta_i)\cos(\phi_L - \phi_i) - n_2\} \leq m \leq \frac{L_b}{\lambda}\{-n_1 \sin(\theta_i)\cos(\phi_L - \phi_i) + n_2\} \tag{A6}$$

$$\frac{-b_m - \sqrt{\Delta}}{2\alpha_m} \leq n \leq \frac{-b_m + \sqrt{\Delta}}{2\alpha_m}. \tag{A7}$$

Given that $n$ and $m$ are integers and are based on Eqs. (A4) and (A5), it can easily be deduced that a finite and discrete set of propagating orders $(n, m)$ will be supported by the diffractive arrangement, which can be directly determined. Finally, the elevation and azimuth angles of propagation, corresponding to the free-space mode $(n, m)$, can be computed from $\theta_d = \arccos\left[k_{t,z}/(k_o n_2)\right]$ and $\phi_d = \arctan\left(k_{t,y}/k_{t,x}\right)$, respectively, with $k_{t,x}$, $k_{t,y}$, and $k_{t,z}$ denoting the $x$, $y$, and $z$ components of $\mathbf{k}_t$.

## APPENDIX B: $\mathcal{PT}$-SYMMETRY-BREAKING TRANSITION IN NON-HERMITIAN OBLIQUE BRAVAIS LATTICES

The effect of $\mathcal{PT}$-symmetry breaking in the operation of the flexible $\mathcal{PT}$-symmetric metasurface can be investigated by studying the dependence of the extinction ratio between mode orders $(-1, -1)$ and $(1, 1)$ on the contrast ratio $\Delta\kappa/\Delta n$, where $\Delta n$ and $\Delta\kappa$ represent the real and imaginary parts of the refractive-index modulation, i.e., $\Delta n = (n_{Al_2O_3} - n_{air})/2$ and $\Delta\kappa = (\kappa_{Ni} - \kappa_{Al_2O_3})/2$. More specifically, by varying the amount of loss (corresponding to the lossy nanopillars) while maintaining the real part of the refractive-index modulation at its nominal value for each wavelength (e.g., $n_{Al_2O_3} = 1.77$ at $\lambda_o = 530$ nm), we obtain the numerical results demonstrated in Fig. S10 in the Supplemental Material [29] for three characteristic wavelengths ($\lambda_o = 450$, 530, and 590 nm) via the finite-element method (FEM). It is evident that the extinction ratio tends to zero for quite small values of loss, while it saturates for large amounts of loss. On the other hand, the extinction ratio tends to zero at $\Delta\kappa/\Delta n \sim 1.7$, independent of the wavelength of operation.

In order to theoretically interpret the aforementioned numerical observations, we provide analytical results for the case of refractive-index modulation of the form $\Delta\hat{n}(\tilde{x}) = \Delta n \cos\tilde{x} + i\Delta\kappa \sin\tilde{x}$ (total refractive-index distribution $n(x) = n_o + i\kappa_o + \Delta\hat{n}(x)$, in which $n_o$ and $k_o$ represent the background real and imaginary refractive indices: see Ref. [19]), where $\tilde{x} = 2\pi x/L$ is the normalized $x$ coordinate. By applying the thin-grating approximation, the transmission factor $T$ (corresponding to the propagation through the bulk arrangement) is given for the Hermitian case ($\Delta\kappa = 0$) by

$$T = e^{ik_o\Delta\hat{n}(\tilde{x})t} = e^{i\Delta n k_o t\cos\tilde{x}} = \sum_{n=-\infty}^{\infty} e^{in\tilde{x}} J_n(\Delta n k_o t) e^{in\pi/2}, \tag{B1}$$

where $k_o$ represents the free-space wave number ($k_o = 2\pi/\lambda_0$) and $t$ corresponds to the thickness of the metasurface (along the direction of propagation). Equation (B1), which can be also viewed as the expansion into Fourier series of the coefficient $T$, is obtained after considering the generator function of the Bessel functions $J_n(q)$, [34]

$$e^{(1/2)q(z-1/z)} = \sum_{n=-\infty}^{\infty} z^n J_n(q), \tag{B2}$$

and setting $z = e^{i(\tilde{x}+\pi/2)}$ and $q = \Delta n k_o t$. From Eq. (B1), since $J_n(q) = J_{-n}(q)$, it can be straightforwardly deduced that the efficiency of the positive orders $(n)$ is identical to the efficiency of the respective negative orders $(-n)$, i.e., the extinction ratio is equivalent to unity. We should note that the ratio $\Delta n t/\lambda_0$ plays an essential role in determining the efficiency of the different diffraction orders, which can be either propagating (if $k_o n_o > 2\pi n/L$) or evanescent (if $k_o n_o \leq 2\pi n/L$) along the direction of propagation (see also Appendix A).

In a similar fashion, by ignoring the real part of the refractive-index modulation ($\Delta\kappa \gg \Delta n$), we obtain for the transmission factor that

$$T = e^{ik_o\Delta\hat{n}(\tilde{x})t} = e^{-\Delta\kappa k_o t\sin\tilde{x}} = \sum_{n=-\infty}^{\infty} e^{in\tilde{x}} I_n(\Delta\kappa k_o t) e^{in\pi/2}. \tag{B3}$$

In this case, we consider the generator function of the modified Bessel functions, [34]

$$e^{(1/2)q(z+1/z)} = \sum_{n=-\infty}^{\infty} z^n I_n(q), \tag{B4}$$

after setting $z = e^{i(\tilde{x}+\pi/2)}$ and $q = \Delta\kappa k_o t$. Since $I_n(q) = I_{-n}(q)$, Eq. (B3) implies that the positive and negative diffraction orders once again have identical efficiencies.

Having examined the marginal cases, now we investigate the far-field diffraction for the $\mathcal{PT}$-symmetric case. After setting $\Delta\kappa = \Delta n$, the refractive-index distribution becomes $\Delta\hat{n}(\tilde{x}) = \Delta n e^{i\tilde{x}}$. By employing the Taylor expansion of the exponential function $e^z = \sum_{n=0}^{\infty} z^n/n!$, we

obtain, for the transfer function,

$$T = e^{ik_o t\Delta n e^{i\tilde{x}}} = \sum_{n=0}^{\infty} \frac{(ik_o t\Delta n e^{i\tilde{x}})^n}{n!} = \sum_{n=0}^{\infty} \frac{(ik_o t)^n \Delta n^n}{n!} e^{in\tilde{x}}. \quad \text{(B5)}$$

Equation (B5) now implies the absence of any negative diffraction orders. In other words, the extinction ratio is now equal to zero and this happens exactly at the $\mathcal{PT}$-breaking transition point ($\Delta\kappa = \Delta n$; see also [19,25,26]). This can also be seen in Fig. S11(a) in the Supplemental Material [29], where we demonstrate extinction-ratio results for different values of $\Delta\kappa/\Delta n$, after calculating numerically the Fourier-series expansion terms for the transmission factor $T = e^{ik_o \Delta\hat{n}(\tilde{x})t}$.

Finally, similar conclusions can be derived in the more generalized 2D $\mathcal{PT}$-symmetric case, where $\Delta\hat{n}(\tilde{x},\tilde{y}) = \Delta\hat{n}_x(\tilde{x}) + \Delta\hat{n}_y(\tilde{y}) = \Delta n_x \cos\tilde{x} + \Delta n_y \cos\tilde{y} + i\Delta\kappa_x \sin\tilde{x} + i\Delta\kappa_y \sin\tilde{y}$, in which $\Delta\hat{n}_x(\tilde{x}) = \Delta n_x \cos\tilde{x} + i\Delta\kappa_x \sin\tilde{x}$ and $\Delta\hat{n}_y(\tilde{y}) = \Delta n_y \cos\tilde{y} + i\Delta\kappa_y \sin\tilde{y}$. For this scenario, the transmission factor now becomes $T(\tilde{x},\tilde{y}) = e^{ik_o\Delta\hat{n}(\tilde{x},\tilde{y})t} = (e^{ik_o\Delta\hat{n}_x t})(e^{ik_o\Delta\hat{n}_y t}) = T_x(\tilde{x})T_y(\tilde{y})$, where $T_x(\tilde{x}) = e^{ik_o\Delta\hat{n}_x t}$ and $T_y(\tilde{y}) = e^{ik_o\Delta\hat{n}_y t}$. As a result, the symmetry properties of $T_x, T_y$, are inherited by $T(\tilde{x},\tilde{y})$. For instance, in the absence of any losses ($\Delta\kappa_x = \Delta\kappa_y = 0$), the efficiencies of the diffraction orders $(n,m)$, $(-n,m)$, $(n,-m)$, and $(-n,-m)$ will all become identical (the indices $n$ and $m$ correspond to the $x$ and $y$ direction, respectively). At the $\mathcal{PT}$-breaking transition point ($\Delta\kappa_x = \Delta n_x, \Delta\kappa_y = \Delta n_y$), we obtain, for the total transfer function [based on Eq. (B5)], that

$$T = e^{ik_o t\Delta n_x e^{i\tilde{x}}} e^{ik_o t\Delta n_y e^{i\tilde{y}}} = \sum_{n=0}^{\infty}\sum_{m=0}^{\infty} \frac{(ik_o t)^{n+m}\Delta n_x^n \Delta n_y^m}{n!m!} e^{in\tilde{x}} e^{im\tilde{y}}. \quad \text{(B6)}$$

Equation (B6) indicates the presence of only the positive orders, while the negative orders are eliminated. The aforementioned observations are also confirmed in Fig. S11(b) in the Supplemental Material [29], where the extinction-ratio results are depicted for different values of the contrast ratios $\Delta\kappa_x/\Delta n_x$ and $\Delta\kappa_y/\Delta n_y$.

By comparing the extinction-ratio curves, as obtained via finite element analysis and the thin-element approximation (see Figs. S10 and S11(a), respectively, in the Supplemental Material [29]), we observe that, qualitatively, they behave similarly with respect to the contrast ratio $\Delta\kappa/\Delta n$ [i.e., the extinction ratio (i) tends to zero at the $\mathcal{PT}$-symmetry breaking point or (ii) tends to unity for $\Delta\kappa/\Delta n \to 0$ and saturates for $\Delta\kappa/\Delta n \gg 1$]. The observed deviation of the optimal point of operation from the theoretically predicted conditions of exact $\mathcal{PT}$-symmetry breaking ($\Delta\kappa/\Delta n = 1$ as evaluated by the thin grating approximation; $\Delta\kappa/\Delta n = 1.7$ as computed numerically via FEM simulations) can be attributed to the fact that our theoretical derivation is merely based on a scalar field approximation. A full vectorial-field calculation (FEM) is required in order to take into account the high-index contrast along with the complex coupling interactions between the successive diffractive nanopillars and their effect on the absolute values of the diffraction efficiencies and the respective extinction ratios (see Ref. [35]). Moreover, the surface (refractive-) index modulation imparted by the scattering nanopillars can only be partially approximated by a sinusoidal distribution, which is intentionally chosen in order to obtain closed-form analytical expressions for the extinction ratio in a variety of cases ($\Delta\kappa/\Delta n = 0$, $\Delta\kappa/\Delta n = 1$, and $\Delta\kappa \gg \Delta n$).


[1] N. Yu, P. Genevet, M. A. Kats, F. Aieta, J.-P. Tetienne, F. Capasso, and Z. Gaburro, Light propagation with phase discontinuities: Generalized laws of reflection and refraction, Science **334**, 333 (2011).

[2] A. V. Kildishev, A. Boltasseva, and V. M. Shalaev, Planar photonics with metasurfaces, Science **339**, 1232009 (2013).

[3] N. Yu and F. Capasso, Flat optics with designer metasurfaces, Nat. Mater. **13**, 139 (2014).

[4] D. Lin, P. Fan, E. Hasman, and M. L. Brongersma, Dielectric gradient metasurface optical elements, Science **345**, 298 (2014).

[5] X. Ni, N. K. Emani, A. V. Kildishev, A. Boltasseva, and V. M. Shalaev, Broadband light bending with plasmonic nanoantennas, Science **335**, 427 (2012).

[6] Y. Yang, W. Wang, P. Moitra, I. I. Kravchenko, D. P. Briggs, and J. Valentine, Dielectric meta-reflectarray for broadband linear polarization conversion and optical vortex generation, Nano Lett. **14**, 1394 (2014).

[7] T. Guo and C. Argyropoulos, Broadband polarizers based on graphene metasurfaces, Opt. Lett. **41**, 5592 (2016).

[8] S. Boroviks, R. A. Deshpande, N. A. Mortensen, and S. I. Bozhevolnyi, Multifunctional metamirror: Polarization splitting and focusing, Acs Photonics **5**, 1648 (2017).

[9] C. M. Bender and S. Boettcher, Real Spectra in Non-Hermitian Hamiltonians Having $\mathcal{PT}$ Symmetry, Phys. Rev. Lett. **80**, 5243 (1998).

[10] R. El-Ganainy, K. G. Makris, M. Khajavikhan, Z. H. Musslimani, S. Rotter, and D. N. Christodoulides, Non-Hermitian physics and PT symmetry, Nat. Phys. **14**, 11 (2018).

[11] T. Kottos, Optical physics: Broken symmetry makes light work, Nat. Phys. **6**, 166 (2010).

[12] G. Castaldi, S. Savoia, V. Galdi, A. Alu, and N. Engheta, $\mathcal{PT}$ Metamaterials via Complex-Coordinate Transformation Optics, Phys. Rev. Lett. **110**, 173901 (2013).

[13] C. E. Rüter, K. G. Makris, R. El-Ganainy, D. N. Christodoulides, M. Segev, and D. Kip, Observation of parity-time symmetry in optics, Nat. Phys. **6**, 192 (2010).

[14] A. Guo, G. Salamo, D. Duchesne, R. Morandotti, M. Volatier-Ravat, V. Aimez, G. Siviloglou, and D. Christodoulides, Observation of $\mathcal{PT}$-Symmetry Breaking in Complex Optical Potentials, Phys. Rev. Lett. **103**, 093902 (2009).

[15] L. Feng, Y.-L. Xu, W. S. Fegadolli, M.-H. Lu, J. E. Oliveira, V. R. Almeida, Y.-F. Chen, and A. Scherer, Experimental demonstration of a unidirectional reflectionless parity-time metamaterial at optical frequencies, Nat. Mater. **12**, 108 (2013).

[16] B. Zhen, C. W. Hsu, Y. Igarashi, L. Lu, I. Kaminer, A. Pick, S.-L. Chua, J. D. Joannopoulos, and M. Soljačić, Spawning rings of exceptional points out of Dirac cones, Nature **525**, 354 (2015).

[17] B. Peng, Ş. K. özdemir, F. Lei, F. Monifi, M. Gianfreda, G. L. Long, S. Fan, F. Nori, C. M. Bender, and L. Yang, Parity–time-symmetric whispering-gallery microcavities, Nat. Phys. **10**, 394 (2014).

[18] K. G. Makris, A. Brandstötter, P. Ambichl, Z. H. Musslimani, and S. Rotter, Wave propagation through disordered media without backscattering and intensity variations, Light Sci. Appl. **6**, e17035 (2017).

[19] Z. Lin, H. Ramezani, T. Eichelkraut, T. Kottos, H. Cao, and D. N. Christodoulides, Unidirectional Invisibility Induced by $\mathcal{PT}$-Symmetric Periodic Structures, Phys. Rev. Lett. **106**, 213901 (2011).

[20] M. Berry, Lop-sided diffraction by absorbing crystals, J. Phys. A **31**, 3493 (1998).

[21] M. Kulishov and B. Kress, Free space diffraction on active gratings with balanced phase and gain/loss modulations, Opt. Express **20**, 29319 (2012).

[22] D. L. Sounas, R. Fleury, and A. Alù, Unidirectional Cloaking Based on Metasurfaces with Balanced Loss and Gain, Phys. Rev. Appl. **4**, 014005 (2015).

[23] R. Fleury, D. L. Sounas, and A. Alu, Negative Refraction and Planar Focusing Based on Parity-Time Symmetric Metasurfaces, Phys. Rev. Lett. **113**, 023903 (2014).

[24] S. Xiao, J. Gear, S. Rotter, and J. Li, Effective PT-symmetric metasurfaces for subwavelength amplified sensing, New J. Phys. **18**, 085004 (2016).

[25] Y. Jia, Y. Yan, S. V. Kesava, E. D. Gomez, and N. C. Giebink, Passive parity-time symmetry in organic thin film waveguides, ACS Photonics **2**, 319 (2015).

[26] C. Hahn, Y. Choi, J. W. Yoon, S. H. Song, C. H. Oh, and P. Berini, Observation of exceptional points in reconfigurable non-Hermitian vector-field holographic lattices, Nat. Commun. **7**, 12201 (2016).

[27] R. Birabassov, A. Yesayan, and T. V. Galstyan, Nonreciprocal diffraction by spatial modulation of absorption and refraction, Opt. Lett. **24**, 1669 (1999).

[28] C. Keller, M. K. Oberthaler, R. Abfalterer, S. Bernet, J. Schmiedmayer, and A. Zeilinger, Tailored Complex Potentials and Friedel's Law in Atom Optics, Phys. Rev. Lett. **79**, 3327 (1997).

[29] See the Supplemental Material at http://link.aps.org/supplemental/10.1103/PhysRevApplied.13.064005 for additional numerical results and a geometric analysis of a generalized oblique Bravais lattice. The diffraction characteristics of a "deformed" and a conventional honeycomb-lattice network are compared and contrasted, along with the respective broadband numerical far-field radiation results. Additional details regarding the experimental methods and setup are also provided.

[30] A. D. Rakić, A. B. Djurišić, J. M. Elazar, and M. L. Majewski, Optical properties of metallic films for vertical-cavity optoelectronic devices, Appl. Opt. **37**, 5271 (1998).

[31] I. Malitson and M. Dodge, Refractive-index and birefringence of synthetic sapphire, J. Opt. Soc. Am. **62**, 1405 (1972).

[32] H.-W. Su and W.-C. Chen, High refractive index polyimide–nanocrystalline-titania hybrid optical materials, J. Mater. Chem. **18**, 1139 (2008).

[33] G. Rhodes, *Crystallography Made Crystal Clear: A Guide for Users of Macromolecular Models* (Elsevier, Burlington, 2010).

[34] M. Abramowitz and I. Stegun, *Handbook of Mathematical Functions* (Dover Publications, New York, 1965).

[35] D. C. O'Shea, T. J. Suleski, A. D. Kathman, and D. W. Prather, *Diffractive Optics: Design, Fabrication, and Test* (SPIE press, Bellingham, 2004), Vol. 62.